Neoproterozoic I-type granites in the Central Tianshan Block (NW China): geochronology, geochemistry, and tectonic implications

SONG Yujia[1], LIU Xijun[1,2,3*], XIAO Wenjiao[2], ZHANG Zhiguo[1], LIU Pengde[1], XIAO Yao[1], LI Rui[1], WANG Baohua[1], LIU Lei[1,3], HU Rongguo[1]

[1] Guangxi Key Laboratory of Hidden Metallic Ore Deposits Exploration, College of Earth Sciences, Guilin University of Technology, Guilin 541004, China;

[2] Xinjiang Research Center for Mineral Resources, Xinjiang Institute of Ecology and Geography, Chinese Academy of Sciences, Urumqi 830011, China;

[3] Collaborative Innovation Center for Exploration of Nonferrous Metal Deposits and Efficient Utilization of Resource, Guilin University of Technology, Guilin 541004, China

Abstract: The Central Tianshan Block is one of numerous microcontinental blocks within the Central Asian Orogenic Belt (CAOB) that overlies Precambrian basement rocks. Constraining the evolution of these ancient basement rocks is central to understanding the accretionary and collisional tectonics of the CAOB, and their place within the Rodinia supercontinent. However, to date, the timing and tectonic settings in which the basement rocks in the Central Tianshan Block formed are poorly constrained, with only sparse geochemical and geochronological data from granitic rocks within the northern segment of the block. Here, we present a systematic study combining U–Pb geochronology, whole-rock geochemistry, and the Sr–Nd isotopic compositions of newly-identified granitic gneisses from the Bingdaban area of Central Tianshan Block. The analyzed samples yield a weighted mean Neoproterozoic $^{206}Pb/^{238}U$ ages of 975–911 Ma. These weakly-peraluminous granitic rocks show a common geochemical I-type granite affinity. The granitic gneisses are calc-alkaline and enriched in large ion lithophile elements (LILEs) and light rare earth elements (LREEs), but they are depleted in high field strength elements (HFSEs); these characteristics are similar to those of typical subduction-related magmatism. All samples show initial $(^{87}Sr/^{86}Sr)_{(i)}$ ratios between 0.705136 and 0.706745. Values for $\varepsilon_{Nd(i)}$ in the granitic gneisses are in the range from –5.7 to –1.2, which correspond to Nd model ages of 2.0–1.7 Ga, indicating a role for Mesoproterozoic to Paleoproterozoic rocks in the generation of the granitic protoliths. The documented geochemical features indicate that the protoliths for the gneisses have a similar petrogenesis and magmatic source, which may reflect partial melting of thickened crust with the addition of small amounts of mantle-derived material. The Central Tianshan Block probably constitute part of an exterior orogen that developed along the margin of the Rodinian supercontinent during the Early Neoproterozoic and underwent a transition from subduction to syn-collision compression at 975–911 Ma.

Keywords: Neoproterozoic I-type granites; geochronology; Central Tianshan Block; Rodinian supercontinent; Central Asian Orogenic Belt (CAOB)

1 Introduction

The Central Asian Orogenic Belt (CAOB), also known as the Altaid tectonic collage, is the largest accretionary orogenic belt in the world (Sengör et al., 1993; Sengör and Natal'in, 1996). It is situated between the Eastern European, Siberian, Tarim, and North China cratons (Fig. 1). It has been widely accepted that the CAOB was formed by successive amalgamation of island arcs, seamounts, oceanic plateaus, accretionary complexes, and numerous Precambrian microcontinents, related to the subduction and closure of the Paleo–Asian Ocean during the Paleozoic era (Coleman, 1989; Jahn et al., 2000; Xiao et al., 2004, 2008a; Long et al., 2011; Rojas-Agramonte et al., 2011). Several Precambrian basement continental blocks, including the Central Tianshan Block, Yili Block in China, Ishim–Middle Tianshan in Kyrgyzstan, and Aktau–Junggar in Kazakhstan, are of importance in understanding the tectonic evolution of the CAOB (Kröner et al., 2013, 2014). Some components of the CAOB record Late Mesoproterozoic to Early Neoproterozoic evolution, which temporally overlaps with the assembly and break-up of the Rodinia supercontinent (Zhang et al., 2012; Gao et al., 2015; Huang et al., 2017). The Chinese Tianshan Orogen is located in the southwestern part of the CAOB (Gao et al., 2015; Xiong et al., 2019), extending from Kazakhstan in the west to Xinjiang Uygur Autonomous Region of China in
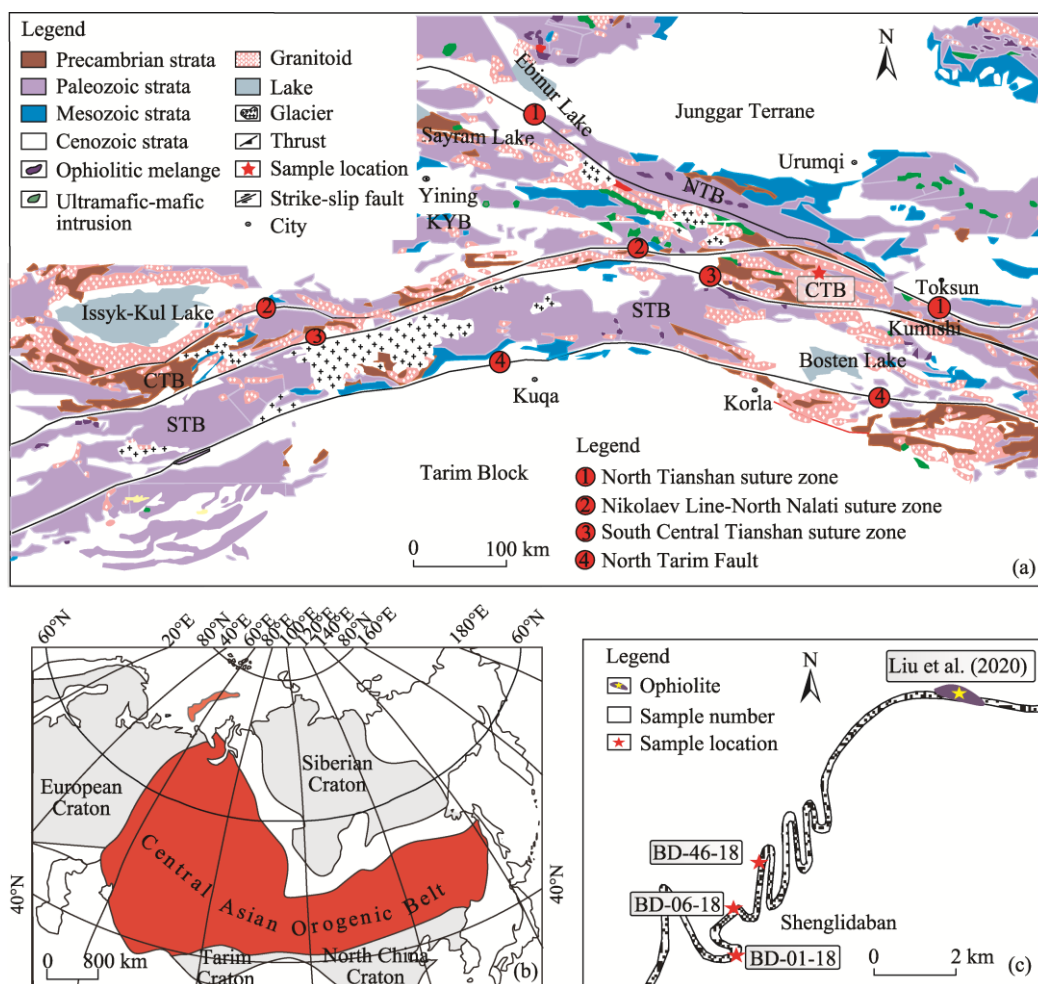
Fig. 1 Geological map of the Central Tianshan Block and adjacent regions (a), and tectonic map of the Central Asian Orogenic Belt (b) as well as sample locations (c). CTB, Central Tianshan Block; KYB, Kazakhstan–Yili Block; NTB, North Tianshan Belt; STB, South Tianshan Belt (modified after Gao et al. (2015) and Liu et al. (2020)).

the east (Yin et al., 2017; Liu et al., 2020). Among several tectonic units within the Chinese Tianshan Orogen, the Central Tianshan Block and the Yili Block are considered as Precambrian microcontinents, which have played a significant role in the process of the accretionary orogen.

The Central Tianshan Block is located between the Tarim, Junggar, and Kazakhstan blocks (Xiao et al., 2009a, 2013; Liu et al., 2020). In recent years, the Early Neoproterozoic granitic rocks have been recognized from several areas within the Central Tianshan Block, including Baluntai, Wuwamen, Bingdaban, Wenquan, Alatage, Pingdingshan, and Xingxingxia. The crystallization ages of these granitic rocks are mainly concentrated between 970 and 806 Ma, and provide a record of the Early Neoproterozoic tectono-magmatic events (Zhang et al., 2005; Yang et al., 2008; Chen et al., 2009; Hu et al., 2010; Gao et al., 2015; Huang et al., 2015a; Huang et al., 2015b, 2017; Meng et al., 2018). Such magmatic events have generally been suggested to be linked with the assembly and break-up of Rodinia (Huang et al., 2017). However, until now, only sparse geochemical and geochronological data have been obtained for Neoproterozoic magmatic rocks from the northern segment of the Central Tianshan Block, especially in the Bingdaban area.

In this paper, we investigate the petrogenesis of Neoproterozoic granites in the Bingdaban area of the Central Tianshan Block by using petrography, zircon U–Pb geochronology, whole-rock geochemistry, and Sr–Nd isotopic compositions of the rocks. We use these data to better understand the age and tectonic environment in which the magmatic rocks formed and discuss the wider implications for the evolution of Rodinia.

2 Geological setting

The Chinese Tianshan Orogen is bordered by the Kazakhstan Tianshan in the west, the Junggar Terrane in the north, and the Tarim Craton in the south (Huang et al., 2015a). It was formed by subduction and accretion of the ancient Tianshan Ocean between the Tarim Craton and the Junggar Block (Xiao et al., 2004, 2009b; Gao et al., 2015). The Chinese Tianshan Orogen is the final collision zone between the Siberian Craton and the Tarim Craton. Therefore, it is an ideal area to reveal the accretion and tectonic history of the CAOB (Xiao et al., 2004, 2008b, 2009a, b). The area experienced a complex history from the Late Mesoproterozoic to the Late Paleozoic. There are many microcontinents in the southwest of the CAOB, including the Central Tianshan Block, the Yili Block in China, and other Precambrian terranes in Kazakhstan and Kyrgyzstan (Gao et al., 2015; Xiong et al., 2019). The Chinese Tianshan Orogen is divided into several main tectonic units: the North Tianshan Belt, the Central Tianshan–Yili Blocks, and the South Tianshan Belt. The North Tianshan, Central Tianshan, and South Tianshan are separated by the North Tianshan and South Tianshan suture zones (Fig. 1a) (Xiao et al., 2004; Gao et al., 2009, 2015; Huang et al., 2015b; Zhu et al., 2019).

Among several tectonic units within the CAOB (Fig. 1a), the North Tianshan Belt and South Tianshan Belt represent two Paleozoic accretionary terranes (Allen et al., 1993; Charvet et al., 2011; Alexeiev et al., 2015; Safonova et al., 2016). The Northern Tianshan Belt represents a Late Paleozoic continental magmatic arc related to south-directed subduction of the northern Tianshan Ocean (Gao et al., 1998; Xiao et al., 2004, 2009a, b). It mainly comprises the Middle Devonian to late Carboniferous shallow marine and terrigenous sedimentary rocks, along with calc-alkaline intermediate to felsic volcanic rocks and ophiolite slices (Wang et al., 2007a, 2011). In the south, the North Tianshan Belt is bounded by the North Tianshan suture zone, and consists of a series of Early Paleozoic ophiolites and related rocks (e.g., the Tangbale, Bingdaban, and Gangou ophiolites). The South Tianshan Belt is located between the Central Tianshan Block and the northern margin of the Tarim Craton. It is a Paleozoic accretionary belt and mainly consists of Paleozoic clastic and volcano-sedimentary rocks (Gao et al., 1998; Long et al., 2011; Wang et al., 2011; Du et al., 2018). It is further characterized by the occurrence of a Carboniferous high-pressure and/or low-temperature metamorphic belt composed of blueschist-, eclogite-, and greenschist-facies metasedimentary rocks, and some mafic meta-volcanic rocks (Gao and Klemd, 2003; Lü et al., 2008; Klemd et al., 2011). Previous studies surmise that the South Tianshan Belt was formed by the northward subduction of the South Tianshan Ocean and amalgamation of the

Central Tianshan Block with the Tarim Block (Gao et al., 1998, 2009; Xiao et al., 2004, 2015; Han et al., 2011).

The Central Tianshan−Yili Blocks are sandwiched between the North Tianshan Belt and South Tianshan Belt, and are bounded by the North Tianshan suture zone to the north and the South Tianshan suture zone to the south (Fig. 1a) (Zhong et al., 2017; Zhu et al., 2019). The Central Tianshan Block is characterized by a Precambrian basement overlain by the Early to Late Paleozoic clastic sedimentary and volcano-sedimentary rocks (Gao et al., 1998, 2009; Hu et al., 2000; Xiao et al., 2004; Yang et al., 2008; Ma et al., 2013). The Precambrian basement consists mainly of Paleoproterozoic to Neoproterozoic granulites, amphibolites, granitic gneisses, banded gneisses, and augen gneisses, along with lower-grade schists, phyllites, quartzites, and marbles (e.g., Gao and Peng, 1985; Hu et al., 1998; He et al., 2012, 2014, 2015; Ma et al., 2013). Two intrusive magmatic episodes at ca. 1.4 Ga and ca. 0.9 Ga have been documented from the Central Tianshan Block (Zhang et al., 2005; Hu et al., 2006, 2010; Chen et al., 2009; Shi et al., 2010; Peng et al., 2012; Huang et al., 2014; He et al., 2015). The Yili Block consists of Precambrian basement rocks that are overlain by Paleozoic arc-related volcanic and sedimentary rocks, and is characterized by the widespread distribution of Early Paleozoic granites within Precambrian basement rocks (Hu et al., 1998; Wang et al., 2007b; Long et al., 2011).
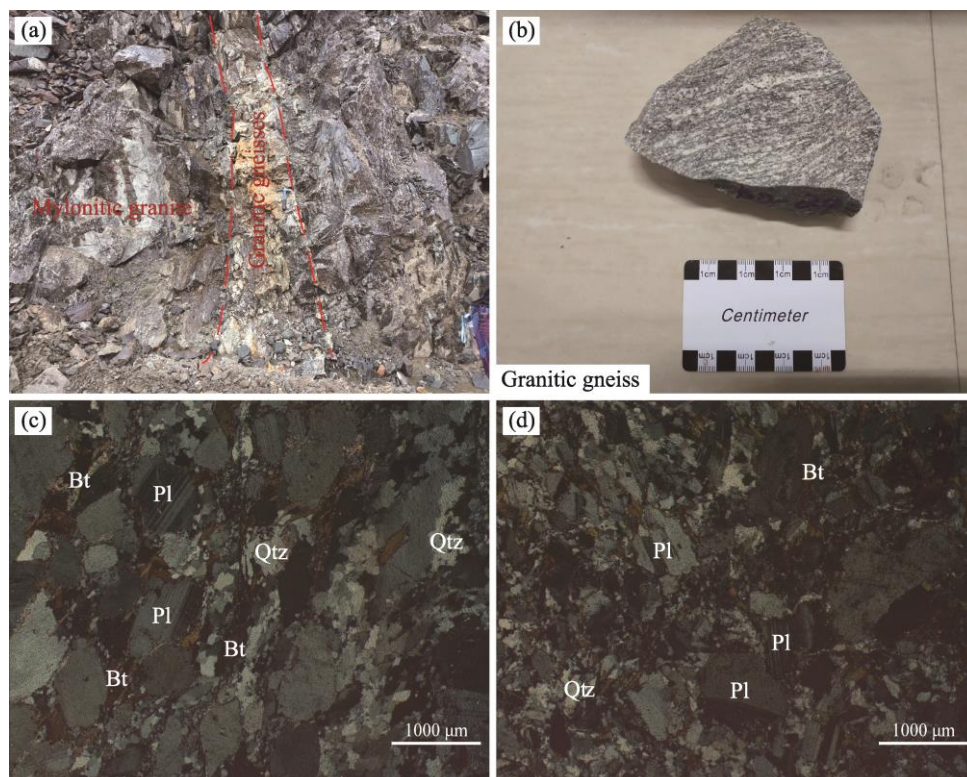
3 Petrography

The study area is located in the Bingdaban area in the northern segment of the Central Tianshan Block (Fig. 2). Granitic rocks mainly crop out between the Hongwuyue Bridge and the No. 1 Glacier on the north side of the Bingdaban area (Liu et al., 2020). The Bingdaban area is mainly composed of two sets of rock assemblages: Precambrian basement rocks and ophiolitic mélanges. The Precambrian basement rocks mainly consist of the Mesoproterozoic to Neoproterozoic augen and banded granitic gneisses, which were intruded by Paleozoic granitoids (Zhu et al., 2007). The study granitic gneisses are mainly located in the Shenglidaban (a high mountain pass), from which three representative samples are selected for zircon dating and geochemical and petrographic analyses (Fig. 1c).
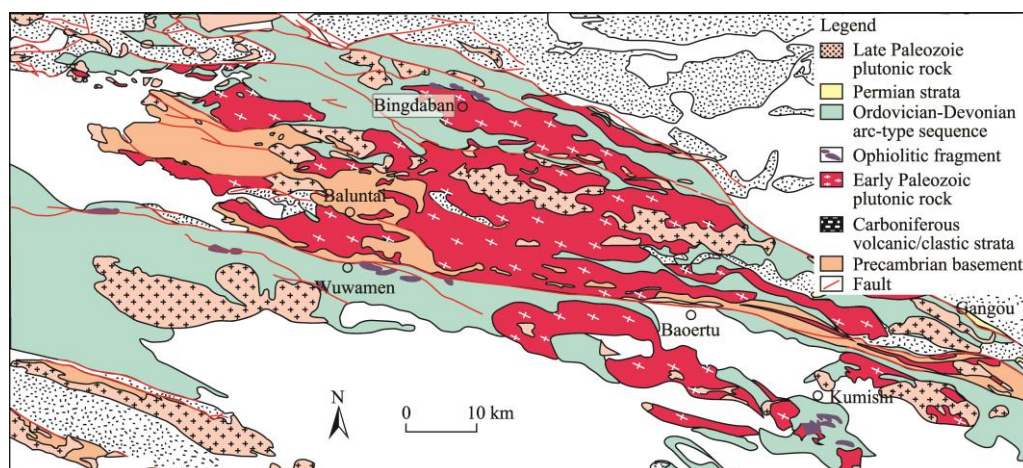
Fig. 2 Simplified geologic map of the Bingdaban area, Central Tianshan Block (modified after Yang et al. (2008) and Liu et al. (2020))

The samples of granitic gneiss are gray and medium-grained, and have a typical granular gneissic texture. They dominantly consist of quartz (volumetric percentage of 30%−40%), K-feldspar (20%−30%), plagioclase (25%−30%), hornblende (approximately 5%), and biotite (approximately 5%), with accessory minerals zircon and magnetite. Biotite and/or muscovite are foliated while quartz and minor feldspar are elongated (Fig. 3).

Fig. 3 Field and petrographic photographs of the studied Neoproterozoic granitic gneisses in the Bingdaban area. (a), field photograph; (b), hand specimens; (c)–(d), photomicrographs. Qtz, Quartz; Pl, Plagioclase; Bt, Biotite.

4   Analytical methods

The U–Pb zircon dating, whole-rock major and trace element, and Sr–Nd isotope analysis were carried out at the Guangxi Key Laboratory of Hidden Metallic Ore Deposits Exploration, Guilin University of Technology, Guilin City, Guangxi Zhuang Autonomous Region, China.

4.1   Zircon U–Pb geochronology

Zircons were separated using standard heavy-liquid and magnetic methods. All zircon grains were imaged using transmitted and reflected light and cathodoluminescence (CL) to reveal internal structures. The CL imaging was obtained using a JXA8230R electron microprobe (JEOL Ltd., Mitaka, Japan). We performed U–Pb zircon dating using laser ablation inductively coupled plasma mass spectrometry (LA-ICP-MS; quadrupole Agilent 7900 ICP-MS (Agilent Technologies Inc., CA, USA) and a GeoLasHD LA system (Coherent Inc., CA, USA) equipped with a 193 nm ArF-excimer laser utilizing the automatic positioning system). The laser spot size was set at 32 μm, laser energy density at 10 J/cm^2, and repetition rate at 10 Hz. Calibrations for the zircon analyses were carried out using United States National Institute of Standards and Technology (NIST) Standard Reference Material NIST610 glass as an external standard and Si as the internal standard. U–Pb isotope fractionation effects were corrected using the Plešovice zircon as the external standard. The TEMORA (417 Ma) zircon was also used as a secondary standard. Isotopic ratios and element concentrations of zircon grains were calculated using GLITTER, and Concordia ages and diagrams were obtained and plotted using Isoplot/Ex 3.0 (Ludwig, 2003). The common lead correction follows the method of Andersen (2002). The reported uncertainty on single data points is reported at the 1σ (σ represents the standard deviation) level, whereas weighted mean ages are reported with uncertainties at the 2σ levels. The U–Pb age data are provided in Table 1.

Table 1 LA-ICP-MS zircon U–Pb isotopic analysis of the granitic gneisses from the Bingdaban area in the Central Tianshan Block

Sample spot	Th (10⁻⁶)	U (10⁻⁶)	Th/ U	Isotopic ratio						Age (Ma)					
				$^{207}Pb/^{206}Pb$	±1σ	$^{207}Pb/^{235}U$	±1σ	$^{206}Pb/^{238}U$	±1σ	$^{207}Pb/^{206}Pb$	±1σ	$^{207}Pb/^{235}U$	±1σ	$^{206}Pb/^{238}U$	±1σ
Sample BD-01-18															
01	833	5167	0.16	0.0708	0.0009	1.6045	0.0262	0.1637	0.0015	954	25	972	10	977	9
02	1051	7802	0.13	0.0698	0.0009	1.5692	0.0268	0.1627	0.0017	924	27	958	11	972	9
03	351	6771	0.05	0.0712	0.0011	1.6006	0.0290	0.1628	0.0016	963	31	970	11	972	9
04	1007	3442	0.29	0.0667	0.0015	1.4980	0.0352	0.1618	0.0018	828	46	930	14	967	10
05	153	624	0.25	0.0675	0.0018	1.5425	0.0434	0.1658	0.0021	854	56	948	17	989	11
06	497	2238	0.22	0.0695	0.0014	1.5588	0.0382	0.1615	0.0019	915	47	954	15	965	11
07	987	10,876	0.09	0.0717	0.0014	1.6177	0.0382	0.1630	0.0023	989	39	977	15	974	12
08	1032	5441	0.19	0.0747	0.0017	1.7052	0.0421	0.1652	0.0017	1061	46	1010	16	986	10
09	2281	7064	0.32	0.0731	0.0013	1.6637	0.0384	0.1645	0.0024	1017	32	995	15	982	13
10	636	1622	0.39	0.0723	0.0017	1.6264	0.0388	0.1629	0.0018	994	47	980	15	973	10
Sample BD-06-18															
01	330	9571	0.03	0.0738	0.0025	1.5996	0.0448	0.1585	0.0028	1037	67	970	18	948	16
02	739	13,358	0.06	0.0686	0.0013	1.5346	0.0331	0.1612	0.0019	887	40	944	13	963	10
03	601	3840	0.16	0.0676	0.0018	1.4961	0.0422	0.1591	0.0020	855	55	929	17	952	11
04	1985	9660	0.21	0.0686	0.0016	1.5409	0.0373	0.1620	0.0019	887	47	947	15	968	11
05	613	3185	0.19	0.0714	0.0016	1.5762	0.0409	0.1591	0.0022	969	47	961	16	952	12
06	958	6379	0.15	0.0695	0.0016	1.5319	0.0390	0.1589	0.0021	915	48	943	16	951	12
07	1050	3678	0.29	0.0678	0.0015	1.4934	0.0354	0.1589	0.0018	861	44	928	14	951	10
08	605	3224	0.19	0.0671	0.0014	1.4759	0.0348	0.1586	0.0018	843	44	921	14	949	10
09	324	6249	0.05	0.0690	0.0016	1.5170	0.0458	0.1592	0.0036	898	48	937	18	952	20
10	510	8641	0.06	0.0709	0.0015	1.5589	0.0359	0.1588	0.0016	954	44	954	14	950	9
11	1075	6424	0.17	0.0702	0.0017	1.5807	0.0406	0.1626	0.0020	1000	48	963	16	971	11
12	536	3584	0.15	0.0660	0.0018	1.4514	0.0411	0.1589	0.0021	807	56	910	17	951	12
13	279	1944	0.14	0.0674	0.0032	1.4266	0.0618	0.1551	0.0025	850	98	900	26	929	14
14	855	6150	0.14	0.0669	0.0016	1.4688	0.0364	0.1589	0.0019	835	49	918	15	951	11
15	560	16,520	0.03	0.0665	0.0014	1.4306	0.0372	0.1553	0.0027	833	39	902	16	931	15
16	506	7731	0.07	0.0658	0.0014	1.4460	0.0346	0.1590	0.0023	798	44	908	14	951	13
17	2874	7997	0.36	0.0660	0.0014	1.4514	0.0356	0.1590	0.0024	806	44	910	15	951	13
18	362	5416	0.07	0.0630	0.0014	1.3894	0.0401	0.1588	0.0030	709	46	884	17	950	17
19	409	5139	0.08	0.0707	0.0015	1.5532	0.0363	0.1588	0.0020	950	44	952	14	950	11
20	678	4453	0.15	0.0674	0.0017	1.5004	0.0388	0.1611	0.0021	852	52	931	16	963	12
21	650	2156	0.30	0.0677	0.0021	1.4826	0.0462	0.1587	0.0021	861	65	923	19	950	11
22	607	1743	0.35	0.0672	0.0022	1.4931	0.0502	0.1612	0.0023	856	67	928	20	964	13
23	950	6663	0.14	0.0671	0.0014	1.4762	0.0356	0.1590	0.0023	843	43	921	15	951	13
24	763	7414	0.10	0.0667	0.0013	1.4362	0.0319	0.1559	0.0019	828	45	904	13	934	11
25	451	4732	0.10	0.0661	0.0012	1.4480	0.0306	0.1588	0.0019	809	44	909	13	950	11
26	2977	9476	0.31	0.0675	0.0012	1.4795	0.0304	0.1587	0.0018	854	42	922	12	949	10
27	709	2595	0.27	0.0686	0.0016	1.4998	0.0389	0.1587	0.0020	887	82	930	16	950	11
28	377	16,764	0.02	0.0686	0.0012	1.5018	0.0325	0.1588	0.0020	887	37	931	13	950	11
29	1719	10,931	0.16	0.0686	0.0014	1.5505	0.0357	0.1630	0.0018	887	43	951	14	974	10
30	359	9742	0.04	0.0689	0.0014	1.5157	0.0374	0.1588	0.0024	894	44	937	15	950	13
31	694	3330	0.21	0.0687	0.0016	1.5585	0.0426	0.1630	0.0023	900	48	954	17	973	13
32	1694	6807	0.25	0.0693	0.0017	1.5252	0.0399	0.1588	0.0019	907	56	941	16	950	11
33	2182	7524	0.29	0.0690	0.0017	1.5258	0.0416	0.1589	0.0021	898	50	941	17	951	12

Continued

Sample spot	Th (10⁻⁶)	U (10⁻⁶)	Th/ U	Isotopic ratio						Age (Ma)					
				$^{207}Pb/$ ^{206}Pb	±1σ	$^{207}Pb/$ ^{235}U	±1σ	$^{206}Pb/$ ^{238}U	±1σ	$^{207}Pb/$ ^{206}Pb	±1σ	$^{207}Pb/$ ^{235}U	±1σ	$^{206}Pb/$ ^{238}U	±1σ
Sample BD-46-18															
01	1012	3661	0.28	0.0702	0.0017	1.4782	0.0451	0.1519	0.0027	1000	51	921	18	911	15
02	397	3350	0.12	0.0741	0.0023	1.5592	0.0535	0.1515	0.0026	1044	58	954	21	910	15
03	1435	6293	0.23	0.0711	0.0017	1.4983	0.0404	0.1515	0.0020	961	50	930	16	909	11
04	488	2787	0.18	0.0700	0.0019	1.4765	0.0425	0.1516	0.0020	929	56	921	17	910	11
05	577	3918	0.15	0.0662	0.0017	1.4019	0.0402	0.1516	0.0024	813	50	890	17	910	14
06	411	3481	0.12	0.0688	0.0018	1.4625	0.0424	0.1518	0.0024	892	54	915	17	911	14
07	469	3019	0.16	0.0690	0.0012	1.4507	0.0296	0.1519	0.0015	900	38	910	12	911	9
08	403	4058	0.10	0.0690	0.0012	1.4496	0.0289	0.1518	0.0015	900	69	910	12	911	9
09	315	3412	0.09	0.0726	0.0018	1.5150	0.0374	0.1516	0.0020	1003	50	936	15	910	11
10	609	5710	0.11	0.0700	0.0016	1.4673	0.0490	0.1516	0.0040	928	47	917	20	910	22
11	457	3872	0.12	0.0702	0.0011	1.4746	0.0280	0.1517	0.0014	1000	33	920	11	910	8
12	1312	2902	0.45	0.0690	0.0018	1.4458	0.0327	0.1531	0.0019	898	53	908	14	918	11
13	362	2747	0.13	0.0678	0.0013	1.4264	0.0325	0.1519	0.0018	861	41	900	14	912	10
14	737	2481	0.30	0.0681	0.0014	1.4290	0.0303	0.1517	0.0016	872	45	901	13	911	9
15	252	1892	0.13	0.0699	0.0015	1.4681	0.0357	0.1515	0.0015	928	46	917	15	910	9
16	641	2534	0.25	0.0683	0.0012	1.4326	0.0297	0.1516	0.0017	880	37	903	12	910	9
17	739	4140	0.18	0.0696	0.0014	1.4575	0.0328	0.1515	0.0019	917	45	913	14	909	10
18	2718	5361	0.51	0.0716	0.0016	1.5030	0.0387	0.1517	0.0020	973	46	932	16	911	11
19	1084	5033	0.22	0.0695	0.0013	1.4598	0.0316	0.1517	0.0015	917	39	914	13	910	9
20	796	5149	0.15	0.0705	0.0015	1.4765	0.0340	0.1516	0.0016	943	43	921	14	910	9
21	617	2884	0.21	0.0719	0.0017	1.5041	0.0392	0.1518	0.0019	983	49	932	16	911	11
22	311	2349	0.13	0.0703	0.0015	1.4729	0.0364	0.1517	0.0019	1000	44	919	15	910	10
23	565	3314	0.17	0.0705	0.0013	1.4980	0.0331	0.1540	0.0019	943	44	930	13	923	10
24	540	3194	0.17	0.0707	0.0014	1.4812	0.0355	0.1516	0.0021	948	40	923	15	910	12
25	752	2950	0.26	0.0706	0.0019	1.4767	0.0431	0.1516	0.0022	946	56	921	18	910	12
26	433	2502	0.17	0.0706	0.0015	1.4826	0.0330	0.1526	0.0018	946	43	923	13	915	10
27	368	3469	0.11	0.0685	0.0012	1.4412	0.0307	0.1524	0.0018	883	32	906	13	914	10
28	226	3699	0.06	0.0746	0.0021	1.5603	0.0447	0.1517	0.0018	1057	58	955	18	910	10
29	652	3893	0.17	0.0729	0.0020	1.5259	0.0444	0.1513	0.0021	1013	49	941	18	908	12
30	1351	3107	0.43	0.0734	0.0022	1.5441	0.0497	0.1517	0.0019	1026	61	948	20	911	11
31	419	3153	0.13	0.0714	0.0023	1.4935	0.0499	0.1518	0.0023	970	67	928	20	911	13
32	218	2382	0.09	0.0719	0.0025	1.5051	0.0531	0.1521	0.0024	983	71	932	22	913	14

Note: LA-ICP-MS, Laser Ablation Inductively Coupled Plasma Mass Spectrometer. σ, standard deviation. Sample BD-01-18, BD-06-18, and BD-46-18 mean granitic gneiss samples in this study.

4.2　Whole-rock major and trace element analyses

The major and trace element compositions (including rare earth element (REE)) of rock samples (*n*=3) were measured at the Guangxi Key Laboratory of Hidden Metallic Ore Deposits Exploration, Guilin University of Technology. Fresh samples were collected and crushed, and then chips were soaked in 4 N hydrochloric acid for half an hour to remove any altered material. The rock chips were then powdered using an alumina ceramic shatterbox. Prior to major element analyses, loss-on-ignition values were measured using a muffle furnace at a constant temperature of 1000℃. The baked samples were then made into glass disks with $Na_2B_4O_7 \cdot 10H_2O$ at approximately 1150℃. An ZSX Primus II X-Ray fluorescence (XRF) instrument (Rigaku, Tokyo, Japan) was used to determine the major element compositions.

Trace element analysis was performed using an Agilent 7900 ICP-MS (Agilent Technologies Inc., CA, USA). Approximately 50 mg of sample powder was dissolved in a bomb with 0.5 mL of

purified HNO_3 and 1.0 mL of hydrofluoric acid (HF), placed into a high-pressure valve, and kept at 190 ℃ for 48 h. After evaporation, 0.5 mL of purified HNO_3 was added to the dry powders; this step was repeated again. We then added 4.0 mL of 4 N purified HNO_3, then placed the bombs into a high-pressure valve and kept them at 170 ℃ for 4 h. Finally, the contents were diluted 1000 times and 10 ng/L of the Rh internal standard was added to correct for signal drift. Before analysis, 8.0–10.0 mL of the solution was pipetted into a clean plastic tube and shaken. The United States Geological Survey standards BHVO, AGV, W-2, and G-2, and national rock standards GSR-1, GSR-2, and GSR-3 were used to calibrate the analyses, and the analytical accuracy was generally better than 2%–5% (Liu et al., 2020). The results are shown in Table 2.

4.3 Whole-rock Sr–Nd isotopic analyses

Whole-rock powders for Sr and Nd isotope analyses were dissolved in Savillex Teflon screw-top capsules by adding 2.0 mL of HF and 1.0 mL of 1:1 HNO_3, and then heated for 5–7 d at 120 ℃ on a hot plate until fully dissolved. The capsules were opened, dried, and added with concentrated HNO_3 to drive out any remaining HF. When drying, 3.0 mL of HNO_3 was added and the capsules were kept warm in 120 ℃ for more than 2 h. Strontium was separated with a SR-B50-A (100–150 μm) resin. REEs were isolated using cation exchange resin (AG50-X8). Finally, Nd was purified using an HDEHP (bis-(2-ethylhexyl) hydrogen phosphate) resin.

The isotope ratio was adjusted to $^{88}Sr/^{86}Sr=8.3752$ and $^{146}Nd/^{144}Nd=0.7219$ to correct for mass fractionation. During the analysis period, instrument stability was assessed using the international standard samples NBS-987 and JNdi-1. The measured values for the NBS-987 Sr and JNdi-1 Nd standards were $^{87}Sr/^{86}Sr=0.710294$ (±0.000016) (n=40; 2SD (standard deviation)) and $^{143}Nd/^{144}Nd=0.512081$ (±0.000008) (n=40; 2SD), respectively. United States Geological Survey reference material BHVO-2 was measured to monitor the accuracy of the analytical procedures, with the following results: $^{87}Sr/^{86}Sr=0.703549$ (±0.000008) and $^{143}Nd/^{144}Nd=0.512965$ (±0.000004) (Liu et al., 2020). The results are shown in Table 3.

5 Results

5.1 Zircon U–Pb geochronology

LA-ICP-MS zircon U–Pb data are given in Table 1, and representative zircon CL images showing the position of analytical spots and $^{206}Pb/^{238}U$ weighted mean ages are shown in Figure 4.

Zircon grains are colorless, and most are characterized by elongated prismatic shapes and lengths ranging from 80 to 200 μm, with ratios of length to width between 1:1 and 3:1. CL images show that the majority of zircon grains have a core-mantle-rim structure. Core and mantle domains generally develop oscillatory zoning, whereas rim domains are structureless and relatively low luminescence, which should be magmatic zircon. The zircon REE patterns are characterized by heavy rare earth element (HREE) enrichment, positive Ce anomalies, and negative Eu and Pr anomalies, indicating a magmatic origin. Some zircons have low Th/U ratios, and some may have undergone degree of metamorphism and/or partial recrystallization (Fig. 4).

5.1.1 Sample BD-01-18

Ten zircons from sample BD-01-18 have U contents of 625×10^{-6}–$10,876\times10^{-6}$ and Th contents of 154×10^{-6}–2282×10^{-6}. U and Th contents are positively correlated, similar to those in magmatic zircon. Ten grains yield concordant $^{206}Pb/^{238}U$ ratios and define a weighted mean $^{206}Pb/^{238}U$ age of 975 (±6) Ma (mean square of weighted deviate (MSWD)=0.530), which is interpreted to represent the crystallization age of the granitic gneiss protolith.

5.1.2 Sample BD-06-18

Thirty-three zircon analyses are tightly clustered on the Concordia and define a weighted mean age of 953 (±4) Ma (MSWD=0.730), which is interpreted as the crystallization age of the granitic gneiss protolith. Grains have U contents of 1893×10^{-6}–6293×10^{-6} and Th contents of 219×10^{-6}–2718×10^{-6}, and U and Th are positively correlated, which is similar to magmatic zircon.

Table 2 Major and trace element compositions of the granitic gneisses from the Bingdaban area in the Central Tianshan Block

Element	Granitic gneisses		
	Sample BD-01-18	Sample BD-06-18	Sample BD-46-18
Major element (%)			
SiO_2	70.89	69.21	70.08
TiO_2	0.32	0.36	0.36
Al_2O_3	14.90	16.30	14.16
$Fe_2O_3^T$	2.04	2.33	2.65
MnO	0.03	0.03	0.06
MgO	0.74	0.86	0.69
CaO	1.69	3.07	1.35
Na_2O	4.57	4.63	3.55
K_2O	3.16	2.32	4.70
P_2O_5	0.08	0.12	0.04
LOI	1.48	0.93	1.46
Total	99.92	100.17	99.10
FeO^T/MgO	2.47	2.44	3.46
K_2O/Na_2O	0.69	0.50	1.32
$Mg^\#$	45.90	46.24	37.74
A/CNK	1.06	1.04	1.06
Trace element ($\times 10^{-6}$)			
Ga	44.10	31.83	30.69
Rb	42.14	32.11	92.32
Sr	87.52	141.29	50.71
Y	4.18	4.08	24.33
Zr	108.96	96.98	133.73
Nb	4.60	4.69	17.13
Ba	417.63	287.87	499.06
La	24.94	21.34	47.81
Ce	49.98	43.07	109.04
Pr	5.35	4.55	12.23
Nd	18.76	15.65	43.40
Sm	3.06	2.57	8.90
Eu	0.69	0.94	0.79
Gd	2.83	2.45	9.63
Tb	0.33	0.32	1.63
Dy	1.45	1.51	8.99
Ho	0.29	0.30	1.71
Er	0.78	0.76	4.78
Tm	0.12	0.11	0.74
Yb	0.82	0.70	5.02
Lu	0.10	0.08	0.60
Hf	4.56	4.06	7.34
Ta	0.86	0.60	4.00
Pb	18.58	33.51	66.35
Th	12.48	8.02	45.63
U	2.73	2.86	12.01
$^a(La/Yb)_N$	21.71	22.02	6.84
$^a(La/Sm)_N$	5.26	5.37	3.47
$^a(Gd/Yb)_N$	2.84	2.91	1.59
ΣREE	109.52	94.32	255.27
LREE	102.78	88.11	222.17
HREE	6.74	6.22	33.10
LREE/HREE	15.25	14.17	6.71
δEu	0.71	1.14	0.26

Note: LOI, loss on ignition; $Mg^\#=100 \times Mg/(Mg+Fe^{2+})$; $FeO^T=0.8998 \times Fe_2O_3^T$; $Fe_2O_3^T$, total Fe; $\delta Eu=Eu/Eu^*=2 \times Eu_N/(Sm+Gd)_N$; A/CNK=molar ($Al_2O_3/(CaO+Na_2O+K_2O)$); A/NK=molar ($Al_2O_3/(Na_2O+K_2O)$); REE, rare earth element; LREE, light rare earth element; HREE, heavy rare earth element. ^{a}, chondrite normalizing values are from Sun and McDonough (1989).

Table 3 Sr–Nd isotopic analysis results of the granitic gneisses from the Bingdaban area in the Central Tianshan Block

Element	Granitic gneisses		
	Sample BD-01-18	Sample BD-06-18	Sample BD-46-18
Rb ($\times 10^{-6}$)	42.10	32.10	92.30
Sr ($\times 10^{-6}$)	87.50	141.0	40.70
Sm ($\times 10^{-6}$)	3.06	2.57	8.90
Nd ($\times 10^{-6}$)	18.80	15.70	43.40
$^{87}Sr/^{86}Sr_{(i)}$	0.706745	0.706647	0.705136
$^{147}Sm/^{144}Nd$	0.100223	0.100817	0.126137
$^{143}Nd/^{144}Nd_{(t)}$	0.511959	0.511977	0.511924
$\varepsilon_{Nd(t)}$	−2.16	−1.20	−5.72
$f_{Sm/Nd}$	−0.49	−0.49	−0.36
T_{DM1} (Ma)	1606	1589	2143
T_{DM2} (Ma)	1730	1704	2038

Note: $^{147}Sm/^{144}Nd$ ratios are calculated using Rb, Sr, Sm, and Nd contents; $\varepsilon_{Nd(t)}=[(^{143}Nd/^{144}Nd_{(t)(sample)}/^{143}Nd/^{144}Nd_{(CHUR)}-1)]\times 10,000$. $\varepsilon_{Nd(t)}$ values are calculated using present-day $(^{147}Sm/^{144}Nd)_{CHUR}=0.1967$ (Jacobsen and Wasserburg, 1980) and $(^{143}Nd/^{144}Nd)_{CHUR}=0.512638$ (Goldstein et al., 1984); T_{DM} values are calculated using present-day $(^{147}Sm/^{144}Nd)_{DM}=0.2137$ and $(^{143}Nd/^{144}Nd)_{DM}=0.51315$ (Peucat et al., 1989).

5.1.3 Sample BD-46-18

Thirty-two analyses are close to the Concordia and define a tight cluster yielding a weighted mean $^{206}Pb/^{238}U$ age of 911 (±4) Ma (MSWD=0.073), which is interpreted to date crystallization of the magmatic protolith. They have U contents of 1893×10^{-6}–6293×10^{-6} and Th contents of 219×10^{-6}–2718×10^{-6}, and U and Th are positively correlated, which is similar to magmatic zircon.

In summary, the granitic gneisses range in age from 975 to 911 Ma, younger than the SHRIMP (sensitive high-resolution ion microprobe) U–Pb age of 926 (±8) Ma obtained by Chen et al. (2009), but older than the age of 969 (±11) Ma obtained by Yang et al. (2008), indicating that the magmatic protoliths of the Bingdaban granitic gneisses are formed during the Neoproterozoic.

5.2 Whole-rock major and trace elements

The major and trace element compositions of representative Bingdaban granitic gneiss samples are listed in Table 2. All the analyzed samples have high SiO_2 (weighted percentage of 69.21%–70.89%) and K_2O+Na_2O (6.95%–8.24%) contents. In a total-alkali versus silica (TAS) diagram, all samples are sub-alkaline igneous rocks and are plotted in the granite field. Values for the alkali saturation index (ASI) (A/CNK=molar $Al_2O_3/(CaO+Na_2O+K_2O)$) vary from 1.04 to 1.06, indicating a calc-alkaline, weakly peraluminous character (Fig. 5). The granitic gneisses have low FeO^T/MgO ratios of 2.44–3.46 with high $Mg^{\#}$ values of 38–46 ($Mg^{\#}=100\times Mg/(Mg+Fe^{2+})$), and therefore resemble magnesian granites.

The granitic gneisses show similar trace elements patterns (Fig. 6a). All are enriched in REEs with total REE concentrations ranging from 94×10^{-6} to 255×10^{-6} (Table 2). In a chondrite-normalized REE diagram (Fig. 6a), the granitic gneisses exhibit enrichment in light rare earth elements (LREEs), $(La/Yb)_N$ in the range of 6.83–22.02, and relatively flat HREE distributions, with $(Gd/Yb)_N$ in the range of 1.59–2.91, negative Eu anomalies (δEu in the range of 0.26–1.14), and significant differentiation between the LREEs ($(La/Sm)_N$ in the range of 3.47–5.37). In a primitive mantle-normalized trace element diagram, the gneisses are characterized by depletion in Nb, Ta, Sr, and Ti, and relatively enriched in large ion lithophile elements (LILEs), such as Rb, U, Th, and Nd (Fig. 6b).
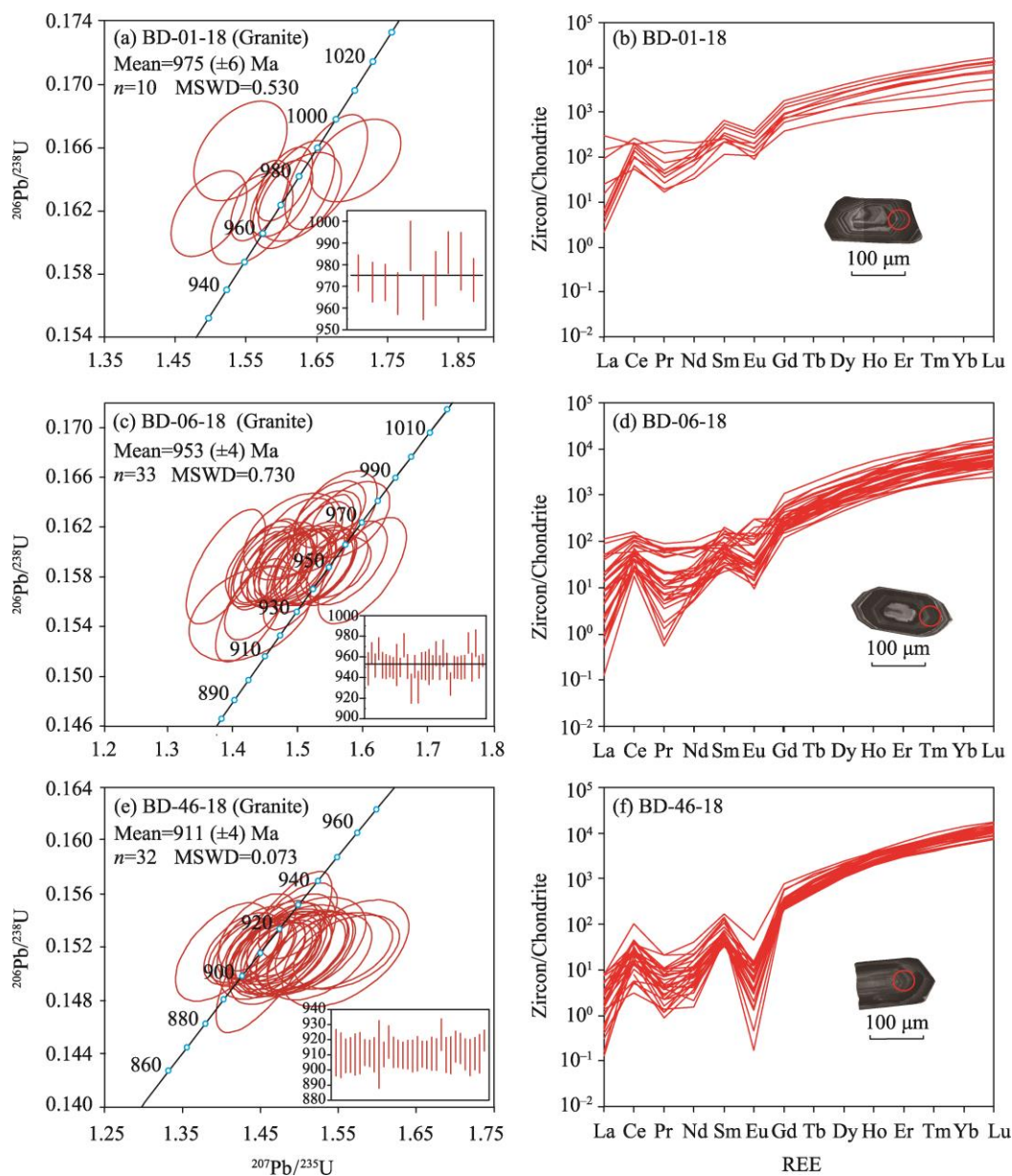
Fig. 4 Concordia diagrams showing zircon U–Pb isotopic analyses (a, c, and e) and chondrite-normalized REE patterns (b, d, and f) from the Bingdaban granitic gneisses in the Central Tianshan Block. REE, rare earth element; MSWD, mean square of weighted deviate.

5.3 Whole-rock Sr–Nd isotopes

Three representative granitic gneiss samples were analyzed to establish their whole-rock Sr–Nd isotopic compositions. The analytical data are listed in Table 3 and plotted in Figure 7. Initial $({}^{87}Sr/{}^{86}Sr)_{(t)}$ ratios for the analyzed samples are between 0.705136 and 0.706745, and $\varepsilon_{Nd(t)}$ values range from –5.7 to –1.2. The fractionation factor ($f_{Sm/Nd}$) values range from –0.49 to –0.36, which are similar to the values of average continental crust (–0.40) (Keto and Jacobsen, 1987). All samples have T_{DM} Nd model ages ranging from 2143 to 1589 Ma, and T_{DM2} Nd model ages varying between 2038 and 1705 Ma. All of granitic gneisses have similar Nd model ages, which correspond to the known age of basement rocks in the Central Tianshan Block (Hu et al., 2000).
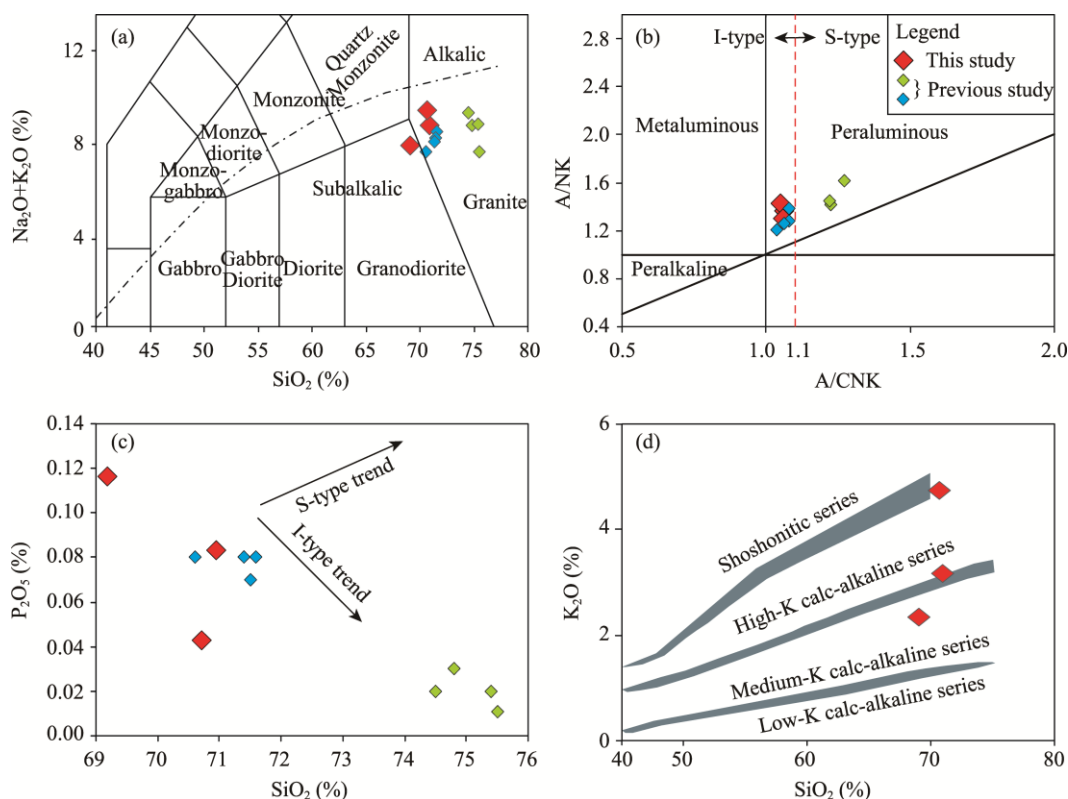
Fig. 5 Total-alkali versus silica diagram (Middlemost, 1994) (a), A/NK versus A/CNK diagram (b) (Maniar and Piccoli, 1989), P_2O_5 versus SiO_2 diagram (c) (Chappell and White, 1992), and SiO_2 versus K_2O diagram (d) (Peccerillo and Taylor, 1976)
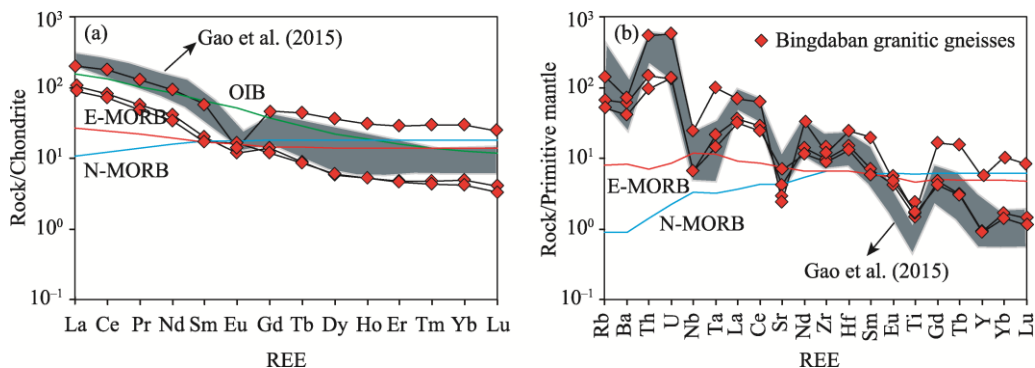

Fig. 6 Chondrite-normalized REE (a) and primitive mantle-normalized trace element diagrams (b) for the studied granitic gneisses. Normalizing values for chondrite and primitive mantle are from Taylor and McLennan (1985) and Sun and McDonough (1989), respectively (reference data from Gao et al. (2015)). N-MORB, normal mid-ocean ridge basalt; E-MORB, enriched mid-ocean ridge basalt; OIB, ocean island basalt. Grey shaded area represents data source from Gao et al. (2015).

6 Discussion

6.1 Granite type

According to different magma sources and mechanisms of formation, granitoids are genetically subdivided into M-type (mantle source), I-type (lower-crustal igneous source), S-type (upper-crustal sedimentary source), and A-type (high-temperature anhydrous) (Chappell and White, 1974; Collins et al., 1982; Chappell, 1999; Chappell and White, 2001; Frost et al., 2001).
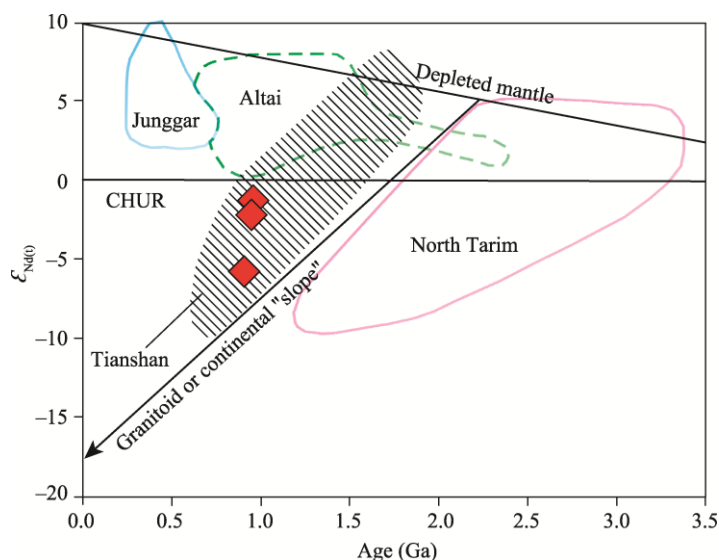
Fig. 7 Plots of $\varepsilon_{Nd(t)}$ versus age for zircons from the studied granitic gneisses in the Central Tianshan Block. The granitoid or continental "slope" is defined with the parameter $f_{Sm/Nd}$=0.4 (indicating the average continental or granitoid isotopic evolution). The Tianshan dashed field represents the isotopic region of Tianshan basement rocks (reference data from the basement rocks in the northern Xinjiang; after Hu et al. (2000)). The isotope fields for the four terranes are distinguished by different colored lines. CHUR, chondritic uniform reservoir.

Three main origins for granites are proposed: (1) a crustal origin; (2) a mantle-derived origin; and (3) a mixed origin that involves both crustal and mantle-derived components (Barbarin, 1999). A-type granites are generated either by fractionation from mantle-derived magmas or interaction between these mantle-derived magmas and continental crust, S-type granites are entirely crustally derived, and I-type granites have a mixed origin (Whalen et al., 1987; Barbarin, 1999). The classification of I-type and S-type granites is based on the properties of the source rocks, while A-type granites are mainly identified on the basis of geochemical indicators, including high FeO^T/MgO ratio and high field strength element (HFSE) contents.

All of the studied samples are medium- to high-K and calc-alkaline series (Fig. 5d) magmatic rocks, which are distinct from M-type granites that have low K_2O contents (<1%) (Bonin, 2007). In addition, all the studied granites have low HFSE contents (e.g., Nb ranging from 4.1×10^{-6} to 17.1×10^{-6} and Zr ranging from 97.0×10^{-6} to 133.0×10^{-6}), which distinguish them from A-type granites. FeO^T/MgO ratios (average of 2.79) in M-type granites are significantly lower than those in typical A-type granites (average of 13.48), but close to those in S-type (average of 2.38) and I-type (average of 2.27) bodies. The mineralogy and geochemical characteristics of the Bingdaban granitic gneisses are consistent with I-type granites. Specifically, the gneisses contain hornblende, but not Al-rich minerals such as cordierite and muscovite, which characterize S-type granites. S-type granites typically contain relatively low SiO_2 contents and are peraluminous, whereas the Bingdaban granitic gneisses have high SiO_2 contents (69.21%–70.89%) and low A/CNK values (between 1.04 and 1.06). In A/CNK diagram, the samples are plotted in the field of I-type granites (Fig. 5b). Furthermore, the granitic gneisses have high K_2O+Na_2O contents (6.95%–8.24%), indicating a calc-alkaline, weakly peraluminous affinity (Fig. 5b and d). P_2O_5 is an effective marker in distinguishing S-type granites from I-type granites. A P_2O_5–SiO_2 diagram shows that P_2O_5 contents decrease with increasing SiO_2 contents, consistent with an I-type origin (Fig. 5c). As the solubility of apatite is different in I-type granites and S-type granites, there is a significant content of P in S-type granites, which increases with fractionation; by contrast, P contents fall to low levels in I-type granites (Chappell, 1999). The Bingdaban granitic gneisses are relatively enriched in light rare earth element (LREE), have relatively flat HREE patterns and negative Eu anomalies (δEu in the range of 0.26–1.14), and exhibit depletion of HFSEs (e.g., Nb, Ta, and Ti) (Fig. 6a and b), consisting with features of subduction-related magmatism. Based on the above

petrographic and geochemical characteristics, we conclude that the protoliths of the Early Neoproterozoic granitic gneisses in the Bingdaban area are I-type granites with medium- to high-K and calc-alkaline.

6.2 Magma source and tectonic setting

Previous studies suggest that I-type granites have a mixed origin, including both crustal- and mantle-derived components (Whalen et al., 1987; Chappell, 1999; Wang et al., 2019). Remelting of sediments by mantle derived from magmas can also form I-type granites (Whalen et al., 1987), and a decrease in the relative contribution of sediment during crustal remelting can lead to the transition from S-type magmas to I-type magmas (Collins et al., 1982). All the studied granite samples show an I-type affinity with weakly-peraluminous characters, negative $\varepsilon_{Nd(t)}$ values (–5.72 to –1.20), and average continental crust-like fractionation factors ($f_{Sm/Nd}$ in the range from –0.49 to –0.36). These geochemical features indicate a similar petrogenesis and magma source for these granitic rocks, which may have formed by partial melting of ancient continental crust (Rudnick, 1995). The whole-rock T_{DM}(Nd) values ranging between 1.7 and 2.0 Ga of the granitic gneisses indicate that Mesoproterozoic to Paleoproterozoic rocks are involved in the generation of the granitic magmas. The observed LREE and LILE enrichment and relative depletion in HFSEs of Nb, Ta, and Ti are thought of as typical 'subduction–signatures'. The crystallization of Ti-rich minerals in the source leads to the depletion of Ti (Foley et al., 2000), which may be related to fractional crystallization of ilmenite. The granitic gneisses have high $Mg^{\#}$ values (38–46), likely related to the addition of mantle-derived materials.

I-type granites can be produced in volcanic arcs, back-arcs, and post-collisional settings. To pinpoint the tectonic setting of magmatism, we use the trace element data with reference to various tectonic discrimination diagrams (Fig. 8). All the granitic gneiss samples have high Sr and low Y contents, suggesting that the continental crust of the Central Tianshan Block had been significantly thickened by approximately 1.0–0.9 Ga, inconsistent with a back-arc setting. In addition, the studied granitic gneisses have high $Mg^{\#}$ values, indicative of a mantle contribution that is common during subduction and following collision. Moreover, the high- to medium-K (calc-alkaline) nature (Fig. 5d) of the rock and their depletion in Nb, Ta, and Ti (Fig. 6b) are consistent with an arc- to syn-collision setting. In an R_1 ($R_1=1000\times(4\times SiO_2/60.09–11\times(Na_2O\times2/61.98+K_2O\times2/94.2)–2\times(Fe_2O_3^T\times2/159.69+TiO_2/79.9)))$ versus R_2 ($R_2=1000\times(6\times CaO/56.08+2\times MgO/40.3+Al_2O_3\times2/101.96))$ discrimination diagram, all samples are plotted within the syn-collision field (Fig. 8a). In a Nb versus Y diagram, the samples fall within the volcanic arc and syn-collisional field (Fig. 8b), which is consistent with the geochemical and isotopic features of the rocks.

6.3 Formation age and geological significance

The Rodinia supercontinent is thought to have amalgamated between 1300 and 900 Ma during the Grenvillian orogenic event and broke-up at 800–700 Ma (Meert and Torsvik, 2003; Li et al., 2008; Zhu et al., 2011; Ma et al., 2013; Gao et al., 2015). Our LA-ICP-MS zircon U–Pb dating shows that protoliths of the Bingdaban granitic gneisses have ages of 975–911 Ma and are the products of a Neoproterozoic tectono–magmatic event in the region. This magmatism may suggest that the Central Tianshan Block was reworked in response to the assembly of Rodinia at 975–911 Ma.

There is widespread evidence for Neoproterozoic granitic magmatism in other parts of the Central Tianshan Block, including a 922 (±8) Ma zircon U–Pb age from the southern part of the Dabaishitou gneissic granites in the Eastern Tianshan (Meng et al., 2018), a 926 (±8) Ma SHRIMP zircon U–Pb age for the Baluntai gneissic granites (Chen et al., 2009), and a 927 Ma Rb–Sr isotopic age for the Pingdingshan gneissic granites (Zhang et al., 2005). In addition, Huang et al. (2017) obtained zircon ages of 918 and 896 Ma from augen and mylonitic gneisses in the eastern Central Tianshan Block, respectively. Huang et al. (2015b) defined age groups at 930–902 and 806 Ma for augen and banded gneisses from the northern Central Tianshan Block along the Nalati–Baluntai road. Gao et al. (2015) constrained zircon U–Pb ages of 903 (±2) and 934 (±1)
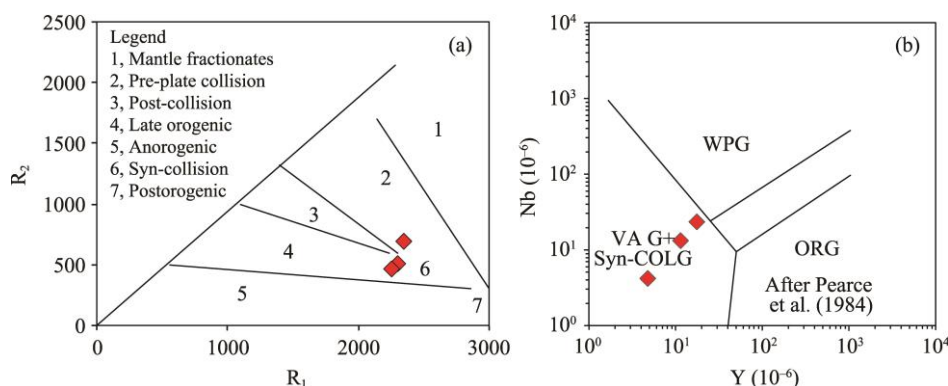
Fig. 8 Major and trace element tectonic discrimination diagrams for the studied granitic gneisses. (a), R_1 versus R_2 diagram of Batchelor and Bowden (1985); (b), Nb versus Y diagram (Pearce et al., 1984). WPG, within plate granitoid; VAG, volcanic arc granitoid; Syn-COLG, syn-collision granitoid; ORG, ocean ridge granitoid. $R_1=1000\times(4\times SiO_2/60.09-11\times(Na_2O\times2/61.98+K_2O\times2/94.2)-2\times(Fe_2O_3^T\times2/159.69+TiO_2/79.9))$ (Batchelor and Bowden, 1985); $R_2=1000\times(6\times CaO/56.08+2\times MgO/40.3+Al_2O_3\times2/101.96)$ (Batchelor and Bowden, 1985).

Ma for gneissic granitoid plutons in the Huoshaoqiao and Wulasutanwutuaiken areas. Moreover, Hu et al. (2006) obtained a 930 Ma zircon age for gneissic granites in the eastern Sayram Lake in the West Tianshan, and 942 (±7) and 919 (±6) Ma SHRIMP U–Pb zircon ages for gneissic granites in the Xingxingxia and Wenquan areas, respectively (Hu et al., 2008; Hu et al., 2010). Furthermore, Huang et al. (2014) carried out an LA-ICP-MS zircon U–Pb study of granitic gneisses in the Alatage and Xingxingxia areas, which yielded weighted mean $^{206}Pb/^{238}U$ ages between 950 and 910 Ma. Huang et al. (2015a) measured the zircon U–Pb age of granitic gneisses formed during a relatively short time period between 970 and 915 Ma in the Alatage and Xingxingxia areas. When considered with existing zircon U–Pb ages from several areas (e.g., Baluntai, Wuwamen, Bingdaban, Wenquan, Alatage, Pingdingshan, and Xingxingxia) in the Central Tianshan Block, we conclude that the formation of the Precambrian basement rocks in the Central Tianshan Block took place mainly in the period between 975 and 806 Ma.

Coeval magmatic rocks have also been recognized in adjacent areas such as the Yili Block in China and Kyrgyz Tianshan. In the Yili Block, for examples, Chen et al. (1999) obtained an 882 (±33) Ma zircon U–Pb ages from intrusions in the northern part of the Laerdundaban gneissic granites; Wang et al. (2014) yielded gneissic granites zircon SHRIMP and LA-ICP-MS U–Pb ages of 919–862 Ma from the northern Yili Block; Xiong et al. (2019) yielded gneissic, augen, and mylonitized granites with U–Pb ages of 947 (±4), 889 (±5), and 892 (±5) Ma, respectively, from the southern Yili Block; Zhu et al. (2019) yielded gneissic granites and mylonitic granodiorites zircon U–Pb ages of 962–934 Ma from the Giergelang area. In the Kyrgyz North Tianshan, Mid-Neoproterozoic ages (844–741 Ma) were documented for the granitoid gneisses (Kröner et al., 2007, 2012), and SHRIMP zircon U–Pb ages of 1186–1045 Ma were obtained for foliated granitoids (Kröner et al., 2013). The ages for the analyzed samples are in accordance with data from regional magmatism in the Central Tianshan Block and adjacent blocks within the CAOB.

The Central Tianshan Block and Yili Block are the two largest Precambrian terranes within the Chinese Tianshan Orogen, but their tectonic and paleogeographic relationships remain unclear. Based on previous studies, the 962–890 Ma granitoids of the Yili Block are mainly I-type and S-type magmatic rocks, whereas the 890–800 Ma granitoids are mainly A-type bodies (Xiong et al., 2019; Zhu et al., 2019). However, although S-type and A-type granites have been reported, I-type granites are rare in the Central Tianshan Block. Our study of I-type granites in the Central Tianshan Block shows that it has a similar tectonic affinity and evolutionary history to the Yili Block, displaying high-K calc-alkaline and arc-related geochemical characteristics with enrichment in LREEs and LILEs and depletion in HREEs and HFSEs, for example, in 945 (±22) Ma biotite granites in the Aktau–Yili (Tretyakov et al., 2015) and 947 (±4) Ma gneissic granites in the Yili Block (Xiong et al., 2019). This further confirms the presence of earliest Neoproterozoic

subduction-related magmatism in these blocks, which may have been related to the assembly of Rodinia.

Large-scale I-type, S-type, and A-type granitic magmatisms in the Central Tianshan Block and adjacent Yili Block were synchronous at 975–806 Ma, indicating a shared history during the Early Neoproterozoic. The observed shift in characteristics likely reflects a transition from subduction to collisional thickening to post-collisional extension associated with Neoproterozoic orogenesis in this region of the CAOB. Thus, the Central Tianshan Block and adjacent Yili Block were likely derived from a single continental plate, which may have been part of the Rodinia supercontinent and involved in its aggregation during the Early Neoproterozoic. Therefore, the Precambrian continental crust blocks (including the Yili Block) in the Central Tianshan Block probably represent continental fragments separated and scattered in the Paleo-Asian Ocean during the Middle- to Late-Neoproterozoic break-up of Rodinia. The Bingdaban granitic gneisses represent the product of partial melting of crustal materials caused by the Greenville orogeny and crustal thickening related to the convergence of the Rodinia supercontinent.

7 Conclusions

This study investigates the petrogenesis of Neoproterozoic granites in the Bingdaban area of the Central Tianshan Block by using studies of petrography, geochronology, and geochemistry. The results indicate that the granitic gneiss yielded the weighted mean $^{207}Pb/^{206}Pb$ ages of 975–911 Ma, suggesting that the protolith of the Bingdaban granitic gneisses were formed in the Neoproterozoic during a widespread tectono-magmatic event. They were I-type granites generated mainly by partial melting of ancient crust with the addition of mantle-derived materials, and most likely were formed during a transition from subduction to syn-collisional compression. We propose that a 975–911 Ma tectono-magmatic event in the Central Tianshan Block corresponds to the assembly of Rodinia, in which granitic gneisses may be the product of partial melting of crustal materials caused by Greenville orogenesis. The Central Tianshan Block shares a similar tectonic affinity and evolutionary history to the Yili Block; both blocks were likely at or near an active continental margin during the assembly of Rodinia.

References

Alexeiev D V, Biske Y S, Wang B, et al. 2015. Tectono-Stratigraphic framework and Palaeozoic evolution of the Chinese South Tianshan. Geotectonics, 49: 93–122.

Allen M B, Windley B F, Zhang C. 1993. Palaeozoic collisional tectonics and magmatism of the Chinese Tien Shan, Central Asia. Tectonophysics, 220(1–4): 89–115.

Barbarin B. 1999. A review of the relationships between granitoid types, their origins and their geodynamic environments. Lithos, 46(3): 605–626.

Batchelor R A, Bowden P. 1985. Petrogenetic interpretation of granitoid rock series using multicationic parameters. Chemical Geology, 48(1–4): 43–55.

Bonin B. 2007. A-type granites and related rocks: Evolution of a concept, problems and prospects. Lithos, 97(1–2): 1–29.

Chappell B W, White A J R. 1974. Two contrasting granite types. Pacific Geology, 8: 173–174.

Chappell B W, White A J R. 1992. I- and S-type granites in the Lachlan Fold Belt. Transactions of the Royal Society of Edinburgh: Earth Sciences, 83(1−2): 1−26.

Chappell B W. 1999. Aluminium saturation in I- and S-type granites and the characterization of fractionated haplogranites. Lithos, 46(3): 535−551.

Chappell B W, White A J R. 2001. Two contrasting granite types: 25 years later. Journal of the Geological Society of Australia, 48(4): 489−499.

Charvet J, Shu L S, Laurent-Charvet S, et al. 2011. Paleozoic tectonic evolution of the Tianshan belt, NW China. Science China Earth Sciences, 54(2): 166−184.

Chen X Y, Wang Y J, Sun L H. 2009. Zircon SHRIMP U−Pb dating of the granitic gneisses from Bingdaban and Laerdundaban (Tianshan Orogen) and their geological significances. Geochimica, 38(5): 424−431. (in Chinese)

Chen Y B, Hu A Q, Zhang G X, et al. 1999. Zircon U−Pb age and its geological significance in the Duku Highway granitic gneiss in the Western Tianshan Mountains. Chinese Science Bulletin, 44(21): 217−325. (in Chinese)

Coleman R G. 1989. Continental growth of northwest China. Tectonics, 8(3): 621−635.

Collins W J, Beams S D, White A J R, et al. 1982. Nature and origin of A-type granites with particular reference to southeastern Australia. Contributions to Mineralogy and Petrology, 80: 189−200.

Du L, Long X P, Yuan C, et al. 2018. Petrogenesis of Late Paleozoic diorites and A-type granites in the central Eastern Tianshan, NW China: Response to post-collisional extension triggered by slab breakoff. Lithos, 318−319: 47−59.

Foley S F, Barth M G, Jenner G A. 2000. Rutile/melt partition coefficients for trace elements and an assessment of the influence of rutile on the trace element characteristics of subduction zone magmas. Geochimica et Cosmochimica Acta, 64(5): 933−938.

Frost B R, Barnes C G, Collins W J, et al. 2001. Transactions of the Royal Society of Edinburgh: Earth Sciences. Journal of Petrology, 42(11): 2033−2048.

Gao J, Li M S, Xiao X C, et al. 1998. Paleozoic tectonic evolution of the Tianshan Orogen, northwestern China. Tectonophysics, 287(1−4): 213−231.

Gao J, Klemd R. 2003. Formation of HP−LT rocks and their tectonic implications in the western Tianshan Orogen, NW China: geochemical and age constraints. Lithos, 66(1−2): 1−22.

Gao J, Long L L, Klemd R, et al. 2009. Tectonic evolution of the South Tianshan orogen and adjacent regions, NW China: geochemical and age constraints of granitoid rocks. International Journal of Earth Sciences, 98(6): 1221−1238.

Gao J, Wang X S, Klemd R, et al. 2015. Record of assembly and breakup of Rodinia in the Southwestern Altaids: Evidence from Neoproterozoic magmatism in the Chinese Western Tianshan Orogen. Journal of Asian Earth Sciences, 113: 173−193.

Gao Z J, Peng C W. 1985. The Precambrian of Tianshan, Xinjiang. Xinjiang Geology, 3(2): 14−25. (in Chinese)

Goldstein S L, O'Nions R K, Hamilton P J. 1984. A Sm−Nd isotopic study of atmospheric dusts and particulates from major river systems. Earth and Planetary Science Letters, 70(2): 221−236.

Han B F, He G Q, Wang X C, et al. 2011. Late Carboniferous collision between the Tarim and Kazakhstan−Yili terranes in the western segment of the South Tian Shan Orogen, Central Asia, and implications for the Northern Xinjiang, western China. Earth-Science Reviews, 109(3−4): 74−93.

He Z Y, Zhang Z M, Zong K Q, et al. 2012. Neoproterozoic granulites from the northeastern margin of the Tarim Craton: Petrology, zircon U−Pb ages and implications for the Rodinia assembly. Precambrian Research, 212−213: 21−33.

He Z Y, Zhang Z M, Zong K Q, et al. 2014. Zircon U−Pb and Hf isotopic studies of the Xingxingxia Complex from Eastern Tianshan (NW China): Significance to the reconstruction and tectonics of the southern Central Asian Orogenic Belt. Lithos, 190−191: 485−499.

He Z Y, Klemd R, Zhang Z M, et al. 2015. Mesoproterozoic continental arc magmatism and crustal growth in the eastern Central Tianshan Arc Terrane of the southern Central Asian Orogenic Belt: Geochronological and geochemical evidence. Lithos, 236−237: 74−89.

Hu A Q, Zhang G X, Zhang Q F, et al. 1998. Constraints on the age of basement and crustal growth in Tianshan Orogen by Nd isotopic composition. Science in China Series D: Earth Sciences, 41(6): 648−657.

Hu A Q, Jahn B M, Zhang G X, et al. 2000. Crustal evolution and Phanerozoic crustal growth in northern Xinjiang: Nd isotopic evidence. Part I. Isotopic characterization of basement rocks. Tectonophysics, 328(1−2): 15−51.

Hu A Q, Wei G J, Deng W F, et al. 2006. 1.4 Ga SHRIMP U−Pb age for zircons of granodiorite and its geological significance from the eastern segment of the Tianshan Mountains, Xinjiang, China. Geochimica, 35(4): 333−345. (in Chinese)

Hu A Q, Jian W G, Zhang J B, et al. 2008. SHRIMP U−Pb ages for zircons of the amphibolites and tectonic evolution significance from the Wenquan domain in the West Tianshan Mountains, Xinjiang, China. Acta Petrologica Sinica, 24(12): 2731−2740. (in Chinese)

Hu A Q, Wei G J, Jahn B M, et al. 2010. Formation of the 0.9 Ga Neoproterozoic granitoids in the Tianshan Orogen, NW China: Constraints from the SHRIMP zircon age determination and its tectonic significance. Geochimica, 39(3): 197–212. (in Chinese)

Huang B T, He Z Y, Zong K Q, et al. 2014. Zircon U–Pb and Hf isotopic study of Neoproterozoic granitic gneisses from the Alatage area, Xinjiang: constraints on the Precambrian crustal evolution in the Central Tianshan Block. Chinese Science Bulletin, 59(3): 287–296.

Huang B T, He Z Y, Zhang Z M, et al. 2015a. Early Neoproterozoic granitic gneisses in the Chinese Eastern Tianshan: Petrogenesis and tectonic implications. Journal of Asian Earth Sciences, 113: 339–352.

Huang Z Y, Long X P, Kröner A, et al. 2015b. Neoproterozoic granitic gneisses in the Chinese Central Tianshan Block: Implications for tectonic affinity and Precambrian crustal evolution. Precambrian Research, 269: 73–89.

Huang Z Y, Long X P, Wang X C, et al. 2017. Precambrian evolution of the Chinese Central Tianshan Block: Constraints on its tectonic affinity to the Tarim Craton and responses to supercontinental cycles. Precambrian Research, 295: 24–37.

Jacobsen S B, Wasserburg G J. 1980. Sm–Nd isotopic evolution of chondrites. Earth and Planetary Science Letters, 50(1): 139–155.

Jahn B M, Wu F Y, Chen B. 2000. Massive granitoid generation in Central Asia: Nd isotope evidence and implication for continental growth in the Phanerozoic. Episodes, 23(2): 82–92.

Keto L S, Jacobsen S B. 1987. Nd and Sr isotopic variations of Early Paleozoic oceans. Earth and Planetary Science Letters, 84(1): 27–41.

Klemd R, John T, Scherer E E, et al. 2011. Changes in dip of subducted slabs at depth: Petrological and geochronological evidence from HP–UHP rocks (Tianshan, NW-China). Earth and Planetary Science Letters, 310(1–2): 9–20.

Kröner A, Alexeiev D V, Hegner E, et al. 2007. Accretionary growth and crust formation in the Central Asian Orogenic Belt and comparison with the Arabian-Nubian shield. Memoir of the Geological Society of America, 200: 181–209.

Kröner A, Alexeiev D V, Hegner E, et al. 2012. Zircon and muscovite ages, geochemistry, and Nd–Hf isotopes for the Aktyuz metamorphic terrane: Evidence for an Early Ordovician collisional belt in the northern Tianshan of Kyrgyzstan. Gondwana Research, 21(4): 901–927.

Kröner A, Alexeiev D V, Rojas-Agramonte Y, et al. 2013. Mesoproterozoic (Grenville-age) terranes in the Kyrgyz North Tianshan: Zircon ages and Nd–Hf isotopic constraints on the origin and evolution of basement blocks in the southern Central Asian Orogen. Gondwana Research, 23(1): 272–295.

Kröner A, Kovach V, Belousova E, et al. 2014. Reassessment of continental growth during the accretionary history of the Central Asian Orogenic Belt. Gondwana Research, 25(1): 103–125.

Li Z X, Bogdanova S V, Collins A S, et al. 2008. Assembly, configuration, and break-up history of Rodinia: A synthesis. Precambrian Research, 160(1–2): 179–210.

Liu X J, Zhang Z G, Xu J F, et al. 2020. The youngest Permian Ocean in Central Asian Orogenic Belt: Evidence from Geochronology and Geochemistry of Bingdaban Ophiolitic Melange in Central Tianshan, northwestern China. Geological Journal, 55(3): 2062–2079.

Long L L, Gao J, Klemd R, et al. 2011. Geochemical and geochronological studies of granitoid rocks from the Western Tianshan Orogen: Implications for continental growth in the southwestern Central Asian Orogenic Belt. Lithos, 126(3–4): 321–340.

Lü Z, Zhang L, Du J, et al. 2008. Coesite inclusions in garnet from eclogitic rocks in western Tianshan, northwest China: Convincing proof of UHP metamorphism. American Mineralogist, 93(11–12): 1845–1850.

Ludwig K R. 2003. User's manual for a geochronological toolkit for Microsoft Excel (Isoplot/Ex version 3.0). Berkeley Geochronology Center, Special Publication, 4: 1–71.

Ma X X, Shu L S, Santosh M, et al. 2013. Paleoproterozoic collisional orogeny in Central Tianshan: Assembling the Tarim Block within the Columbia supercontinent. Precambrian Research, 228: 1–19.

Maniar P D, Piccoli P M. 1989. Tectonic discrimination of granitoids. Geological Society of America Bulletin, 101(5): 635–643.

Meert J G, Torsvik T H. 2003. The making and unmaking of a supercontinent: Rodinia revisited. Tectonophysics, 375(1–4): 261–288.

Meng Y, Tang S L, Wang K, et al. 2018. Zircon U–Pb age, geochemistry and tectonic implications of Neoproterozoic granite from south of Dabaishitou, East Tianshan. Earth Science, 43(12): 4427–4442. (in Chinese)

Middlemost E A K. 1994. Naming materials in the magma/igneous rock system. Earth-Science Reviews, 37(3–4): 215–224.

Pearce J A, Harris N B W, Tindle A G. 1984. Trace element discrimination diagrams for the tectonic interpretation of granitic rocks. Journal of Petrology, 25(4): 956–983.

Peccerillo A, Taylor S R. 1976. Geochemistry of eocene calc–alkaline volcanic rocks from the Kastamonu area, Northern

Turkey. Contributions to Mineralogy and Petrology, 58(1): 63–81.

Peng M X, Zhong C G, Zuo Q H, et al. 2012. The ages of the gneissic granite from Kawabulag area in the Eastern Tianshan and their geological significances. Xinjiang Geology, 30: 12–18. (in Chinese)

Peucat J J, Vidal P, Bernard-Griffiths J, et al. 1989. Sr, Nd and Pb isotopic systematics in the Archaean low- to high-grade transition zone of southern India: Synaccretion vs. post-accretion Granulites. Journal of Geology, 97(5): 537–549.

Rojas-Agramonte Y, Kroner A, Demoux A, et al. 2011. Detrital and xenocrystic zircon ages from Neoproterozoic to Palaeozoic arc terranes of Mongolia: Significance for the origin of crustal fragments in the Central Asian Orogenic Belt. Gondwana Research, 19(3): 751–763.

Rudnick R L. 1995. Making continental crust. Nature, 378(6557): 571–578.

Safonova I, Biske G, Romer R L, et al. 2016. Middle Paleozoic mafic magmatism and ocean plate stratigraphy of the South Tianshan, Kyrgyzstan. Gondwana Research, 30: 236–256.

Sengör A M C, Natal'in B A, Burtman V S. 1993. Evolution of the Altaid tectonic collage and Palaeozoic crustal growth in Eurasia. Nature, 364(6435): 299–307.

Sengör A M C, Natal'in B A. 1996. Turkic-type orogeny and its role in the making of the continental crust. Annual Review of Earth and Planetary Sciences, 24(1): 263–337.

Shi W X, Liao Q A, Hu Y Q, et al. 2010. Characteristics of Mesoproterozoic granites and their geological significances from Middle Tianshan Block, East Tianshan district, NW China. Geological Science and Technology Information, 29(1): 29–37. (in Chinese)

Sun S S, McDonough W F. 1989. Chemical and isotopic systematics of oceanic basalts: Implications for mantle composition and processes. Geological Society London Special Publications, 42(1): 313–345.

Taylor S R, Mclennan S M. 1985. The continental crust: Its composition and evolution. Journal of Geology, 94(4): 57–72.

Tretyakov A A, Degtyarev K E, Shatagin K N, et al. 2015. Neoproterozoic anorogenic rhyolite-granite volcanoplutonic association of the Aktau-Mointy sialic massif (Central Kazakhstan): Age, source, and paleotectonic position. Petrology, 23(1): 22–44.

Wang B, Chen Y, Zhan S, et al. 2007a. Primary Carboniferous and Permian paleomagnetic results from the Yili Block (NW China) and their implications on the geodynamic evolution of Chinese Tianshan Belt. Earth and Planetary Science Letters, 263(3–4): 288–308.

Wang B, Shu L S, Cluzel D, et al. 2007b. Geochemical constraints on Carboniferous volcanic rocks of the Yili Block (Xinjiang, NW China): Implication for the tectonic evolution of Western Tianshan. Journal of Asian Earth Sciences, 29(1): 148–159.

Wang B, Shu L S, Faure M, et al. 2011. Paleozoic tectonics of the southern Chinese Tianshan: Insights from structural, chronological and geochemical studies of the Heiyingshan ophiolitic mélange (NW China). Tectonophysics, 497(1–4): 85–104.

Wang B, Liu H S, Shu L S, et al. 2014. Early Neoproterozoic crustal evolution in northern Yili Block: Insights from migmatite, orthogneiss and leucogranite of the Wenquan metamorphic complex in the NW Chinese Tianshan. Precambrian Research, 242: 58–81.

Wang G H, Wang Z Z, Yan C M. 2019. A survey of the genesis classification and geochemical diagram discrimination of granite. Yunnan Geology, 38(1): 28–37. (in Chinese)

Whalen J B, Currie K L, Chappell B W. 1987. A-type granites: geochemical characteristics, discrimination and petrogenesis. Contributions to Mineralogy & Petrology, 95(4): 407–419.

Xiao W J, Zhang L C, Qin K, et al. 2004. Paleozoic accretionary and collisional tectonics of the eastern Tianshan (China): Implications for the continental growth of central Asia. American Journal of Science, 304(4): 370–395.

Xiao W J, Windley B F, Yong Y, et al. 2008a. Early Paleozoic to Devonian multiple-accretionary model for the Qilian Shan, NW China. Journal of Asian Earth Sciences, 35(3–4): 323–333.

Xiao W J, Han C M, Yuan C, et al. 2008b. Middle Cambrian to Permian subduction-related accretionary orogenesis of Northern Xinjiang, NW China: Implications for the tectonic evolution of central Asia. Journal of Asian Earth Sciences, 32(2–4): 102–117.

Xiao W J, Windley B F, Yuan C, et al. 2009a. Paleozoic multiple subduction-accretion processes of the southern Altaids. American Journal of Science, 309(3): 221–270.

Xiao W J, Windley B, Huang B, et al. 2009b. End-Permian to mid-Triassic termination of the accretionary processes of the southern Altaids: implications for the geodynamic evolution, Phanerozoic continental growth, and metallogeny of Central Asia. International Journal of Earth Sciences, 98(6): 1189–1217.

Xiao W J, Windley B F, Allen M B, et al. 2013. Paleozoic multiple accretionary and collisional tectonics of the Chinese Tianshan orogenic collage. Gondwana Research, 23(4): 1316–1341.

Xiao W J, Windley B F, Sun S, et al. 2015. A tale of amalgamation of three Permo-Triassic Collage Systems in Central Asia: Oroclines, Sutures, and Terminal Accretion. Annual Review of Earth and Planetary Sciences, 43(1): 477–507.

Xiong F H, Hou M C, Cawood P A, et al. 2019. Neoproterozoic I-type and highly fractionated A-type granites in the Yili Block, Central Asian Orogenic Belt: Petrogenesis and tectonic implications. Precambrian Research, 328: 235–249.

Yang T N, Li J Y, Sun G H, et al. 2008. Mesoproterozoic continental arc type granite in the Central Tianshan Mountalins: Zircon SHRIMP U–Pb dating and geochemical analyses. Acta Geologica Sinica (English Edition), 82(1): 117–125.

Yin J Y, Chen W, Xiao W J, et al. 2017. Geochronology, petrogenesis, and tectonic significance of the latest Devonian–early Carboniferous I-type granites in the Central Tianshan, NW China. Gondwana Research, 47: 188–199.

Zhang D Y, Zhang Z C, Encarnaci ón J, et al. 2012. Petrogenesis of the Kekesai composite intrusion, western Tianshan, NW China: Implications for tectonic evolution during late Paleozoic time. Lithos, 146–147: 65–79.

Zhang Z Z, Gu L X, Yang H, et al. 2005. Characteristics and genesis of the Pingdingshan mega-augen gneissic granite in the eastern Tianshan Mountain areas. Acta Petrologica Sinica, 21(3): 879–908. (in Chinese)

Zhong L L, Wang B, Alexeiev D V, et al. 2017. Paleozoic multi-stage accretionary evolution of the SW Chinese Tianshan: New constraints from plutonic complex in the Nalati Range. Gondwana Research, 45: 254–274.

Zhu W B, Charvet J, Xiao W J, et al. 2011. Continental accretion and intra-continental deformation of the Central Asian Orogenic Belt. Journal of Asian Earth Sciences, 42(5): 769–773.

Zhu X Y, Wang B, Cluzel D, et al. 2019. Early Neoproterozoic gneissic granitoids in the southern Yili Block (NW China): Constraints on microcontinent provenance and assembly in the SW Central Asian Orogenic Belt. Precambrian Research, 325: 111–131.

Zhu Y F, Zhou J, Zeng Y. 2007. The Tianger (Bingdaban) shear zone hosted gold deposit, west Tianshan, NW China: Petrographic and geochemical characteristics. Ore Geology Reviews, 32(1–2): 337–365.